



Microstructures and Mechanical Properties of a Newly Developed Austenitic Heat Resistant Steel

Peng Liu^{1,2} · Zhao-Kuang Chu¹ · Yong Yuan³ · Dao-Hong Wang⁴ · Chuan-Yong Cui¹ · Gui-Chen Hou¹ · Yi-Zhou Zhou¹ · Xiao-Feng Sun¹

Received: 24 March 2018 / Revised: 28 April 2018 / Published online: 25 June 2018
© The Chinese Society for Metals and Springer-Verlag GmbH Germany, part of Springer Nature 2018

Abstract

The effect of heat treatment on the microstructures and mechanical properties of a newly developed austenitic heat resistant steel (named as T8 alloy) for ultra-supercritical applications have been studied. Results show that the main phases in the alloy after solution treatment are γ and primary MX . Subsequent aging treatment causes the precipitation of $M_{23}C_6$ carbides along the grain boundaries and a small number of nanoscale MX inside the grains. In addition, with increasing the aging temperature and time, the morphology of $M_{23}C_6$ carbides changes from semi-continuous chain to continuous network. Compared with a commercial HR3C alloy, T8 alloy has comparable tensile strength, but higher stress rupture strength. The dominant cracking mechanism of the alloy during tensile test at room temperature is transgranular, while at high temperature, intergranular cracking becomes the main cracking mode, which may be caused by the precipitation of continuous $M_{23}C_6$ carbides along the grain boundaries. Typical intergranular cracking is the dominant cracking mode of the alloy at all stress rupture tests.

Keywords Austenitic heat resistant steel · Microstructure · Mechanical property · Fracture mode

1 Introduction

Improving efficiency and reducing pollution have always been the goal pursued in the field of thermal power technology [1]. Increasing steam service temperature and pressure has been regarded as the most effective way to improve thermal efficiency [2, 3]. At present, the steam temperature and steam pressure of the ultra-supercritical (USC) unit have been raised above 600 °C and 25 MPa, respectively [4–6]. However, the raising of steam parameters deteriorates the working environment of high-

temperature structural materials of USC unit further. It is known that super-heater and re-heater tubes are operated at the highest temperature range in USC power plants. Therefore, new requirements for the properties of the materials are also put forward: long-term rupture strength (100 MPa for 10⁵ h), steam corrosion and oxidation resistance [7]. Nowadays, advanced austenitic heat resistant steels are the most suitable material for super-heater and re-heater tubes in USC power plants in the view of superior long-term high-temperature strength, excellent oxidation/corrosion resistance, as well as the relatively low cost [5, 8].

At present, some existing traditional austenitic heat resistant steels, such as TP347H, Super304H and HR3C, have been generally used for super-heater and re-heater tubes. TP347H is an austenitic heat resistant steel of Type 18Cr–8Ni fabricated by adding Nb into TP304H steel, which is based on NbC phase precipitation strengthening. However, inadequate Cr addition makes it more susceptible to intergranular corrosion, and its resistance to oxidation and spallation is also limited [9]. Super304H is similar to TP347H except for the additions of 3 wt% Cu and 0.1 wt% N. It has excellent creep resistance, due to the

Available online at <http://link.springer.com/journal/40195>

✉ Chuan-Yong Cui
chycui@imr.ac.cn

- ¹ Institute of Metal Research, Chinese Academy of Sciences, Shenyang 110016, China
- ² School of Materials Science and Engineering, University of Science and Technology of China, Hefei 230026, China
- ³ Xi'an Thermal Power Research Institute Co. Ltd., Xi'an 710032, China
- ⁴ Jiangsu Feiyue Pump Group Co. Ltd., Taizhou 225300, China

strengthening of finely dispersed Cu-rich phases. However, its unqualified match of C and Nb induces the high intergranular corrosion susceptibility of the Super304H tubes [10]. HR3C is an austenitic heat resistant steel of Type 25Cr–20Ni developed by adding Nb and N into the TP310 steel, which is mainly strengthened by the finely dispersed *MX* and *Z* phases. The 25 wt% Cr content of HR3C ensures better corrosion/oxidation resistance as compared to conventional 18Cr–8Ni series alloys [11]. But the strengthening effects of *MX* and *Z* phases cannot satisfy the strength requirement at higher temperatures, and the strengthening mechanism of *Z* phase requires a more comprehensive understanding [12, 13]. In the light of the above analysis, the austenitic heat resistant steels currently used for the super-heater and re-heater tubes all have some limitations, and therefore, it is necessary to develop new alloys to meet the operating requirements of USC units.

A new 25Cr–20Ni type austenitic heat resistant steel (named as T8 alloy) which contains high contents of C (0.17 wt%) and Co (1.96 wt%) has been recently developed and studied in the present study. Preliminary explorations have been conducted on the effects of solution treatment and aging treatment on the microstructure, especially the distribution and morphology of the precipitated phases. The tensile properties and fracture modes at room temperature, 650 and 750 °C, have been studied. Meanwhile, the stress rupture properties and fracture modes of T8 alloy tested at various conditions have also been studied.

2 Experimental

The chemical composition (wt%) of the T8 alloy is listed in Table 1. The 23.6 wt% Cr is for the consideration of good oxidation resistance at high temperatures beyond 650 °C. The 19.5 wt% Ni is intended to stabilize the austenite matrix while suppressing the precipitation tendency of the σ phase. The 0.58 wt% Nb and 0.23 wt% N are expected to form fine *MX* type compound [CrNbN and Nb(C,N)], while the 0.17 wt% C is expected to form fine $M_{23}C_6$ type carbides ($M = \text{Fe, Cr}$) in this steel [14]. The purpose of adding 0.002 wt% B is to improve the intergranular corrosion resistance of the material. The 1.96 wt% Co is intended to stabilize austenite, inhibit coarsening of alloy carbides, enhance the binding energy of solid solution lattice, and cooperate with other alloying elements in the steel to play the role of precipitated strengthening phase [3, 15].

The T8 alloy was prepared by vacuum induction melting, homogenized at 1150 °C for 2 h and subsequently 1200 °C for 24 h and air-cooled. Then, the ingot was forged and rolled into a 15-mm thick plate at 1100 °C and cooled in air. All the test specimens used in this study were cut from this plate along the longitudinal direction. Solution treatment was carried out at 1230 °C for 30 min, followed by water quenching. Subsequent aging treatments were conducted at 750 and 800 °C for 0.5 and 4 h, respectively, and followed by air cooling. Specimens with 4 mm in gauge diameter and 20 mm in gauge length were tensile tested at a strain rate of $3.0 \times 10^{-4} \text{ s}^{-1}$ at room temperature, 650 °C and 700 °C, respectively. Stress rupture tests were carried out on the specimens with 8 mm in gauge diameter and 30 mm in gauge length at 650–750 °C and 110–250 MPa. All the tensile specimens were machined from solid solution-treated specimens.

Phases of the specimens were analyzed using X-ray diffraction (XRD) method. The microstructures were analyzed by optical microscopy (OM) and scanning electron microscopy (SEM) equipped with energy dispersive spectrometer (EDS). The specimens for microstructural analysis were ground, polished and finally etched with 25 ml $\text{H}_2\text{O} + 25 \text{ ml HCl} + 5 \text{ g CuSO}_4 \cdot 5 \text{ H}_2\text{O}$. The phases were also studied by transmission electron microscopy (TEM) with the aid of JEM 2100 TEM operating at 200 kV. The TEM foils were prepared by traditional mechanical grinding and electro-polishing. The electro-polishing was performed at about 20 V and $-30 \text{ }^\circ\text{C}$ in a solution of 10 vol% perchloric acid and 90 vol% ethanol. The phase transformation was also investigated by thermodynamic calculations on the platform of JMatPro software (Version7.0).

3 Results and Discussion

3.1 Thermodynamic Calculations

Figure 1 shows the equilibrium phase diagram simulated by JMatPro software (general steel database). The main precipitated phases are $M_{23}C_6$ carbide, $M_2(\text{C,N})$, *MN*, γ and σ phases. *MN* phases form during solidification process, while topologically close-packed (TCP) phases, such as σ , precipitate below 700 °C.

Table 1 Chemical composition (wt%) of T8 alloy

Ni	Cr	Nb	Si	N	C	B	P	Co	V	Fe
19.5	23.6	0.58	0.46	0.23	0.17	0.002	0.027	1.96	0.1	Bal.

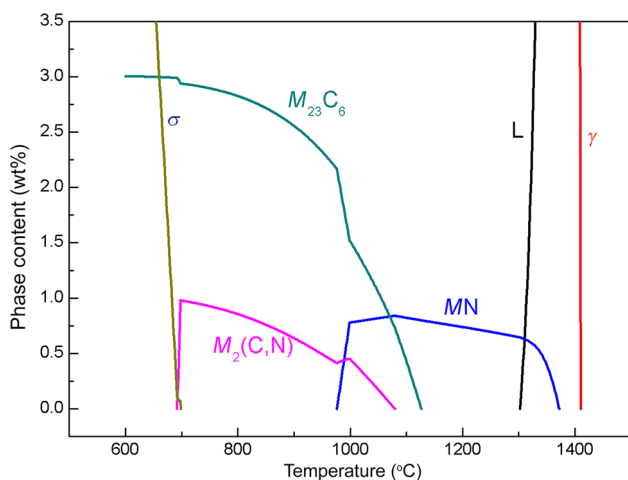


Fig. 1 Predicted equilibrium phase diagram of alloy

3.2 Phases and Microstructures

XRD pattern of T8 alloy after solution treatment is illustrated in Fig. 2. T8 alloy is mainly composed of an austenite matrix phase of $\text{Cr}_{0.19}\text{Fe}_{0.7}\text{Ni}_{0.11}$ (at.%). The microstructure of T8 alloy after solution treatment is shown in Fig. 3a. Large austenite grains with a small number of secondary phases distributing both inside the grains and at the grain boundaries can be clearly seen in the alloy. Due to their negligible amount, XRD analysis fails to detect them. TEM morphology and selected area electron diffraction (SAED) pattern analysis (Fig. 3b) show that these secondary phases were identified as *MX* phases. EDS analysis (Fig. 3c) of *MX* phases notes that *M* is mostly substituted for Nb. Additionally, a number of annealing twins in the grains are observed. The twin boundaries in the austenite grains can ameliorate the plasticity of the alloy by interrupting the continuity of the austenite grain boundaries and

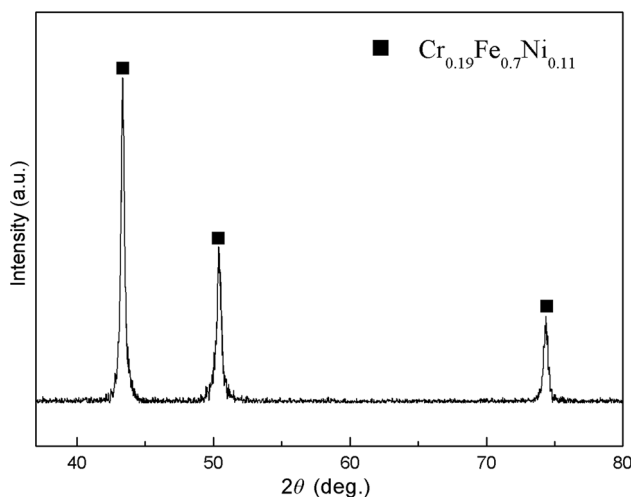


Fig. 2 XRD pattern of alloy after solution treatment

relaxing the stress at the austenite grain boundaries [14]. The average grain size of the T8 alloy is approximately $65\ \mu\text{m}$, which is close to that of commercial HR3C alloy. The size of undissolved primary bulk *MX* phases in T8 alloy is about $1\text{--}8\ \mu\text{m}$, while the solution-treated HR3C is mainly composed of an austenite matrix as well as an irregular-shaped prime Z phase inside the grains with a size of $100\text{--}200\ \text{nm}$ [12].

In general, the purpose of the solution treatment is to obtain moderate grain size and dissolve the secondary phases. Aging treatment is subsequent re-precipitation process to optimize the morphology and size of the precipitation phases [16]. The precipitates in aged HR3C steel are continuous network of $M_{23}C_6$ carbides along the austenite grain boundaries, dispersed Z phase with a size of $20\text{--}200\ \text{nm}$, and *MX* phases inside the grains. After long-term aging, σ precipitation at the grain boundary will weaken the mechanical properties [17]. Based on thermodynamic calculations (Fig. 1), the aging treatments of T8 alloy were conducted at 750 and $800\ ^\circ\text{C}$ for 0.5 and $4\ \text{h}$, respectively, to enable the precipitation of strengthening phases and avoid the precipitation of TCP phases. Figure 4 shows the microstructures of the alloy after different aging treatments. Primary bulk *MX* phases and a small number of new *MX* precipitates with a size of $200\text{--}300\ \text{nm}$ are observed after 750 and $800\ ^\circ\text{C}$ aging treatment. The vast majority of *MX* phases randomly distribute in the grains and a small amount at the grain boundaries. In addition, it can be clearly seen that different phase precipitates along the grain boundaries after aging treatment. TEM morphology, SAED pattern, and EDS composition analysis of the grain boundary precipitates are presented in Fig. 5. The results indicate that grain boundary precipitates are mainly $M_{23}C_6$ carbides where *M* is mainly substituted for Cr, Fe. In addition, $M_{23}C_6$ carbide has a coherent relationship with the matrix and its lattice constant is three times of that of the matrix. The orientation relationship between the $M_{23}C_6$ carbide and the matrix is $[001]_{M_{23}C_6} // [001]_{\text{Matrix}}$ as shown in the SAED pattern in Fig. 5a. The distribution and morphology of $M_{23}C_6$ carbides along the grain boundaries after different aging treatments are shown in Fig. 6. The precipitation of $M_{23}C_6$ carbides along the austenite grain boundaries can be observed after $750\ ^\circ\text{C}$ aging treatment for different aging time. In addition, with the aging time increasing from 0.5 to $4\ \text{h}$, the morphology of $M_{23}C_6$ carbides changes from semi-continuous chain to continuous network. After aged at $800\ ^\circ\text{C}$ for $0.5\ \text{h}$, continuous network of $M_{23}C_6$ carbides forms along the austenite grain boundaries. With the aging time increasing from 0.5 to $4\ \text{h}$, the thickness of $M_{23}C_6$ carbides increases due to coarsening of continuous network of the carbides.

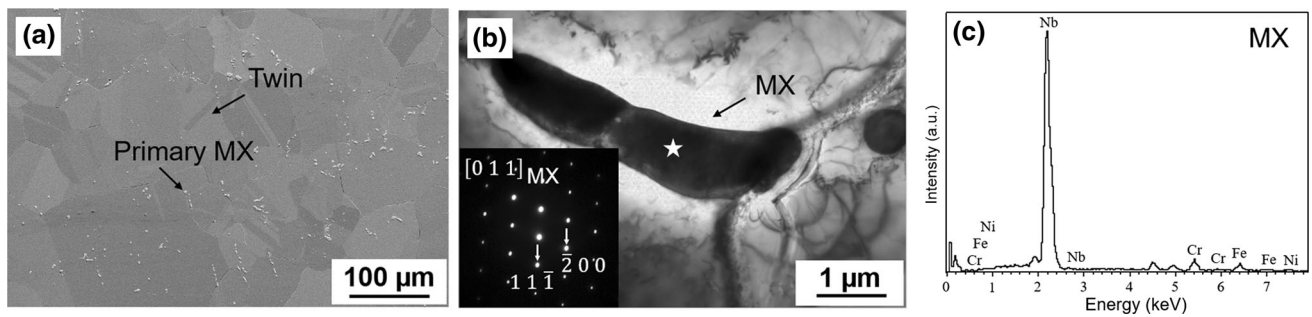


Fig. 3 **a** Image of T8 alloy illustrating twin and *MX* phase in grains, **b** TEM morphology of *MX* phase, and corresponding SAED pattern (inset) **c** EDS result from position of pentagram in Fig. 3b

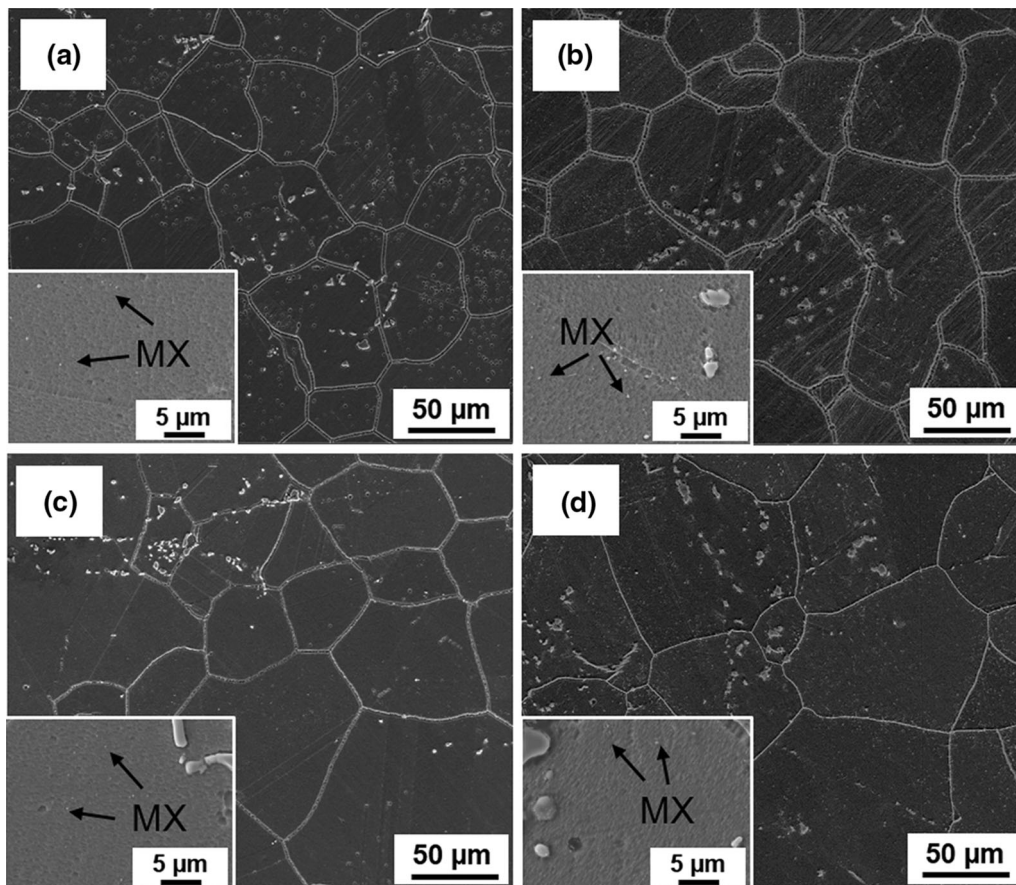


Fig. 4 Microstructures of alloy after different aging treatments (the inset image is the higher magnification figure of nanoscale *MX* phases): **a** 750 °C, 0.5 h; **b** 750 °C, 4 h; **c** 800 °C, 0.5 h; **d** 800 °C, 4 h

3.3 Tensile Properties

It is widely known that continuously distributed $M_{23}C_6$ carbides induced by aging treatment weaken the mechanical properties [14, 18, 19]. In addition, as mentioned above, only a small number of nanoscale *MX* phases precipitate after aging treatment. Therefore, the tensile tested and stress rupture tested samples are only treated by solid solution.

Table 2 shows the tensile results of T8 and HR3C alloys tested at various temperatures. The data of HR3C alloy are obtained from Ref. [11]. The results show that T8 alloy has comparable yield and ultimate strength. However, the elongation of T8 alloy is lower than that of HR3C alloy at high temperatures. The room temperature elongation of 61% indicates excellent ductility, but the tensile ductility dramatically decreases with temperature increasing up to 700 °C. The increase in the test temperature leads to the decrease of both strength and ductility of the alloy.

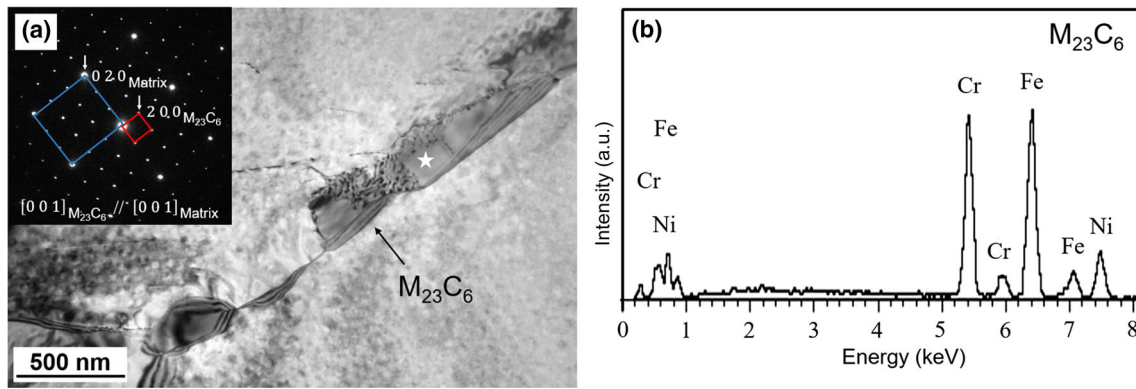


Fig. 5 **a** TEM morphology of $M_{23}C_6$ carbides along grain boundaries and corresponding SAED pattern (inset), **b** EDS result from position of pentagram in Fig. 5a

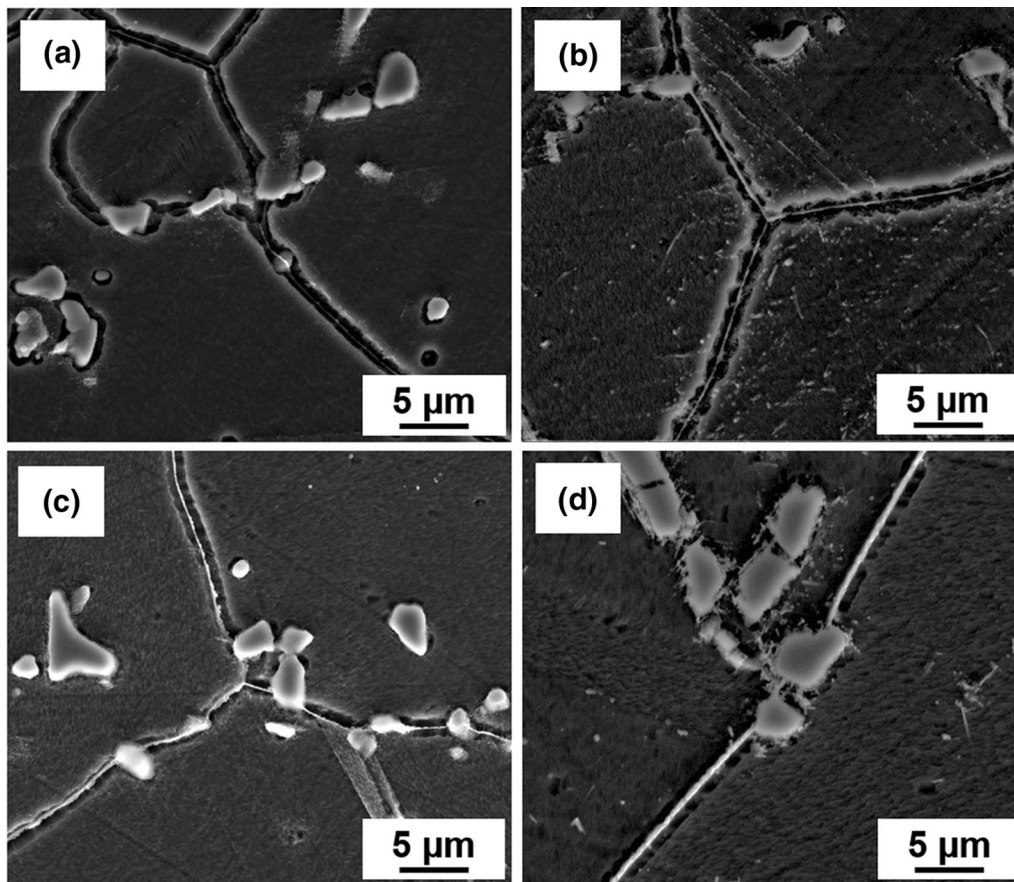


Fig. 6 Distribution and morphology of $M_{23}C_6$ carbides along grain boundaries after different aging treatments: **a** 750 °C, 0.5 h; **b** 750 °C, 4 h; **c** 800 °C, 0.5 h; **d** 800 °C, 4 h

Table 2 Tensile test results of T8 and HR3C alloys at room temperature (25 °C), 650 and 700 °C

Test temperature (°C)	Yield strength (MPa)		Ultimate tensile strength (MPa)		Elongation (%)	
	T8	HR3C	T8	HR3C	T8	HR3C
25	333	350	756	750	61	50
650	179	200	508	500	30	39
700	187	190	443	450	21	30

The fracture surfaces and the longitudinal sections of the tensile tested samples at different temperatures are presented in Figs. 7 and 8, respectively. Plenty of dimples and secondary intergranular cracking on the fracture surface of the specimen tested at room temperature can be observed in Fig. 7a, d. The low binding strength of the irregular blocky *MX* phases and the austenite matrix leads to a large number of *MX* phases peeling off during the tensile test at room temperature. The fracture surface of the specimen tested at 650 °C (Fig. 7b, e) shows typical intergranular cracking characteristics. Secondary intergranular cracking and a few dimples can be observed in Fig. 7e. The fracture surface obtained at 700 °C (Fig. 7c, f) is similar to that obtained at 650 °C, but the dimples are hardly observed.

The crack propagation exhibits a mixed mode during tensile test at room temperature, as clearly illustrated in Fig. 8a. The examination of longitudinal section shows that transgranular cracking is a dominant cracking mechanism at room temperature. Figure 8d shows that grains are elongated approximately along the tensile stress direction at room temperature. A large number of slip bands within the grains indicate that significant grain deformation occurs during the tensile test at room temperature [11, 20, 21], which is confirmed by the large elongation of 61% at room temperature. However, grain deformation causes a great number of grain boundaries parallel with the direction of stress direction. As a result, the expansion path of intergranular cracking is longer and shear stress is smaller compared with transgranular cracking, resulting in the dominating presence of transgranular cracking [22, 23].

A small portion of transgranular path length can be observed in the longitudinal section of fracture surface at 650 °C (Fig. 8b) while no transgranular cracking at 700 °C (Fig. 8c). This indicates that the grain boundary provides a convenient path for the crack propagation at high temperatures. The longitudinal section of fracture surfaces obtained at 650 °C (Fig. 8e) and 700 °C (Fig. 8f) reveals that the secondary crack has a primary development at the grain boundary. A small number of *MX* phases with a size of 200–300 nm inside the grains and the continuous $M_{23}C_6$ carbides along the austenite grain boundaries precipitate during the tensile tests at 650 and 700 °C. The precipitation of nanometer scale *MX* phases is beneficial to improve the strength of T8 alloy. According to the thermodynamic theory of stress effect on the phase equilibrium, applied tensile stress decreases the solubility of C and Cr elements in austenitic matrix [24–26]. In addition, with the increase in dislocation density in austenitic matrix during the tensile test, C and Cr elements may segregate in the stress concentration locations [27]. Therefore, the precipitation of $M_{23}C_6$ carbides at the grain boundaries is further promoted during the high-temperature tensile test. On the one hand, the precipitation of $M_{23}C_6$ carbides during the high-temperature tensile test leads to the formation of the Cr depletion area adjacent to the carbides, which reduces the solid solution strengthening effect [10, 14]. Besides, the precipitation of continuous $M_{23}C_6$ at the grain boundary increases the tendency of intergranular cracking [27]. The slip band can hardly be found in the grains after the tensile tests at 650 and 700 °C. This leads to the decline of the

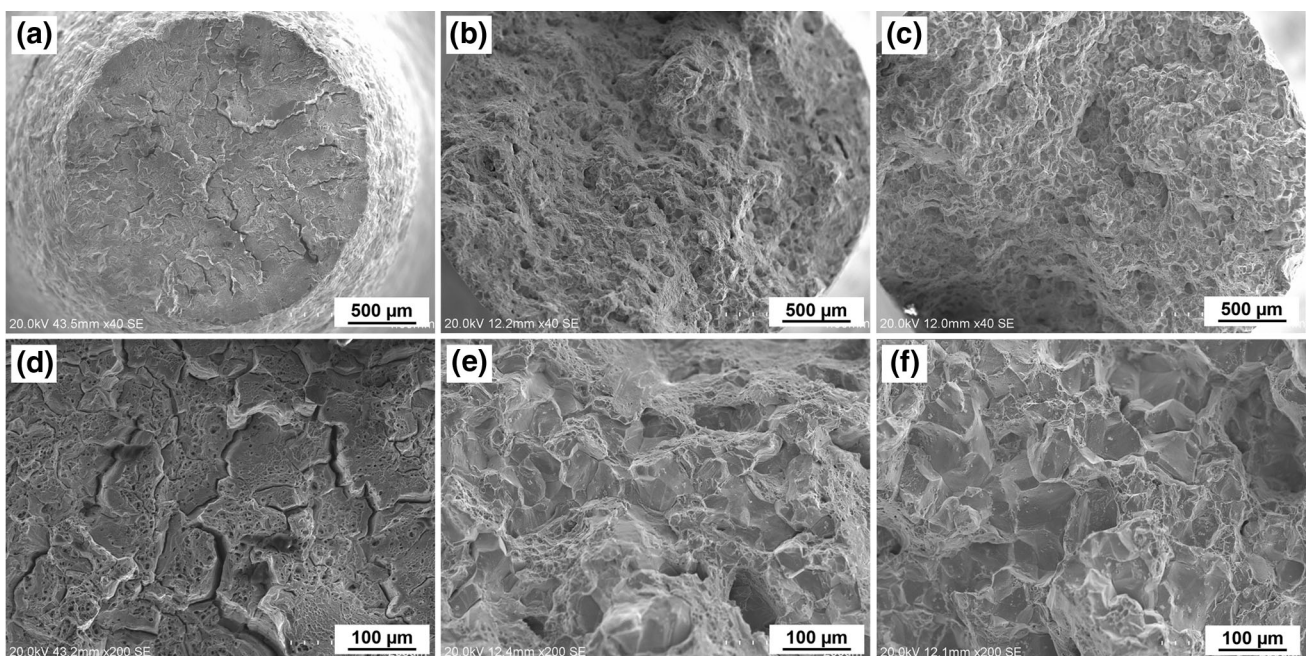


Fig. 7 Fracture surfaces of tensile tests under room temperature **a, d**, 650 °C **b, e**, 700 °C **c, f** at low **a-c**, high **d-f** magnification

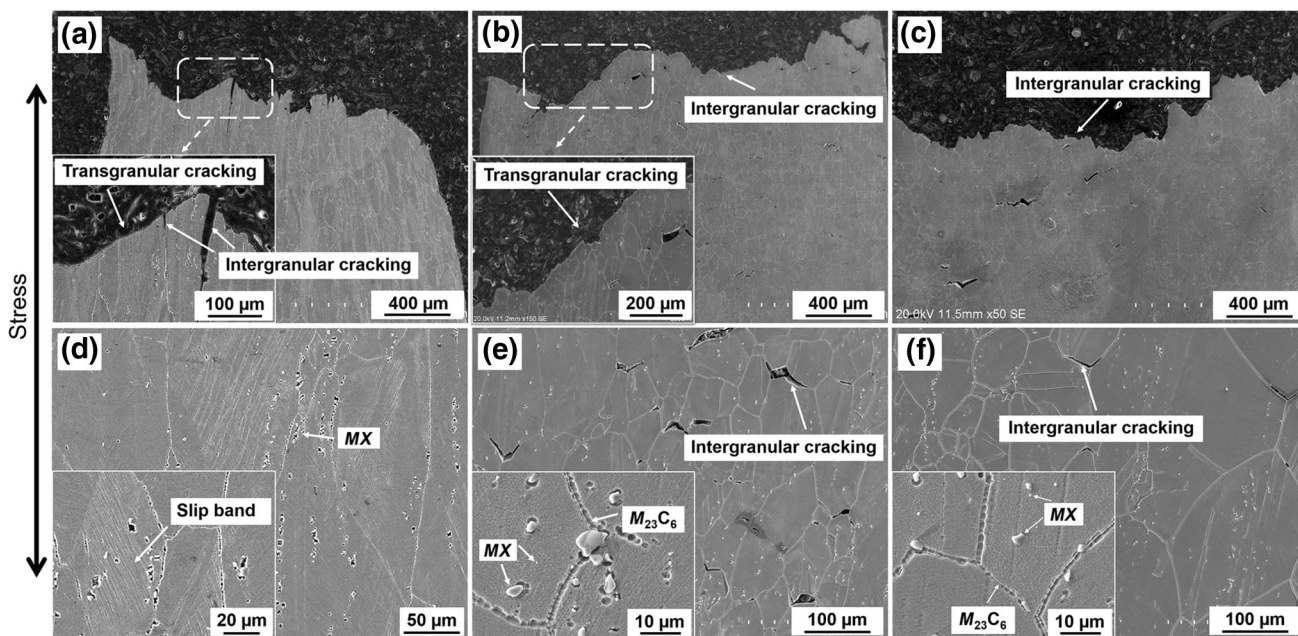


Fig. 8 Longitudinal section of fracture surfaces of tensile tests under room temperature **a, d**, 650 °C **b, e**, 700 °C **c, f** at low **a-c**, high **d-f** magnification

grain strength, which might be the main reason responsible for the decrease in the alloy strength at high temperatures. However, the dominating presence of typical intergranular cracking indicates that the strength of carbide/matrix interface is lower than the strength inside the grain at 650 and 700 °C. As a result, the crack primarily nucleates and propagates at the interface between the continuous $M_{23}C_6$ carbides and the austenite matrix during the tensile tests at 650 and 700 °C. According to the predicted equilibrium phase diagram of the alloy (Fig. 1), $M_{23}C_6$ carbide fraction reaches the highest value and almost does not change at the temperature below 700 °C. Thus, the impact of $M_{23}C_6$ carbides dissolution on the grain strength and the influence of $M_{23}C_6$ carbides content on grain boundaries during the temperature increasing are so small that they can be neglected. These are confirmed by the small difference between the tensile mechanical properties of 650 and 750 °C.

3.4 Stress Rupture Properties

The stress rupture properties of T8 and HR3C alloys at various conditions are shown in Table 3. The data of HR3C alloy are obtained from Ref. [28]. At 650 °C/250 MPa, 700 °C/180 MPa, and 750 °C/130 MPa, the rupture lives of T8 alloy are almost 1.4 times than that of HR3C alloy. And the rupture elongations of T8 alloy are comparable with those of HR3C alloy at various conditions. The Larson–Miller parameters (LMPs) of HR3C alloy [28] and T8 alloy are shown in Fig. 9, which shows that the stress

Table 3 Stress rupture properties of T8 and HR3C alloys tested at various conditions

Test condition	Life (h)		Elongation (%)	
	T8	HR3C	T8	HR3C
650 °C/250 MPa	1409	988	9	9
700 °C/180 MPa	685	500	17	19
750 °C/130 MPa	567	398	24	23

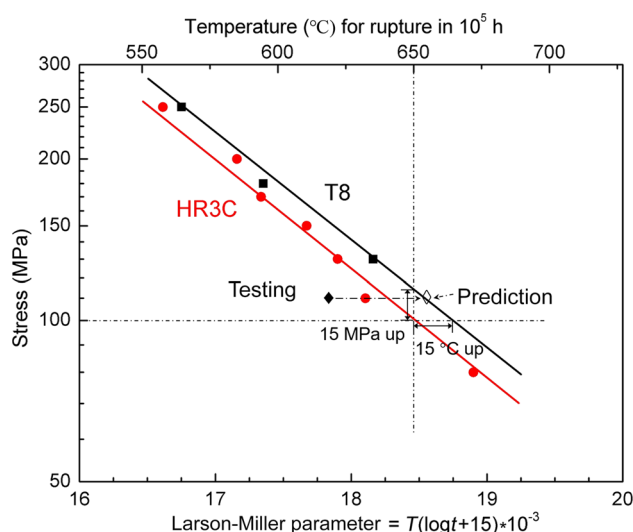


Fig. 9 Larson–Miller parameters of T8 and HR3C alloys (T temperature; t time)

rupture resistance of T8 alloy is better than that of HR3C alloy. In addition, a temperature gain of 15 °C could be expected for T8 alloy compared with HR3C alloy at the required stress of 100 MPa. And the stress rupture strength of T8 is extrapolated to approximately 100 MPa after 10^5 h at 650 °C which is 15 MPa higher than that of HR3C.

The fracture surfaces and longitudinal section of fracture surfaces after stress rupture tests at various conditions are presented in Fig. 10. Typical intergranular failure mode occurs at all stress ruptured specimens, which is consistent with tensile fracture mode at high temperatures. Furthermore, the tensile strain rate plays a very important role in determining the T_E , the temperature of the grain interior strength equivalence to grain boundary strength. Higher tensile strain rate leads to a higher T_E [1]. Above the T_E , the grain boundary strength is lower than the grain interior strength. The strain rate during tensile test is a constant ($3.0 \times 10^{-4} \text{ s}^{-1}$) and much higher than that of the stress rupture test. Combined with the tensile fracture features at high temperatures, it can be deduced that T_E for the stress

rupture test is lower than 650 °C, thus leading to a typical intergranular failure mode. In addition, the direction of intergranular crack propagation is basically vertical to the stress loading direction. A number of secondary cracks have a primary development at the grain boundary in all stress ruptured samples.

Higher magnification images of the longitudinal section of the fractures are shown in Fig. 10g, h, i. A large number of *MX* phases with a size of about 500 nm dispersedly precipitated inside the grains in all stress ruptured samples. And the nanometer scale *MX* phases are the main strengthening precipitates in the matrix after long-time creep. At 700 °C/180 MPa (Fig. 10e), large-size cracks form at the edge of the stress ruptured sample, while cracks in sample center region are much smaller, which may be due to formation at different stages during the stress rupture test. With the increase in rupture life, widening and coarsening of grain boundaries can be clearly observed in Fig. 10d, e, f. Under the action of applied stress, the interface between the precipitates (*MX* particles and

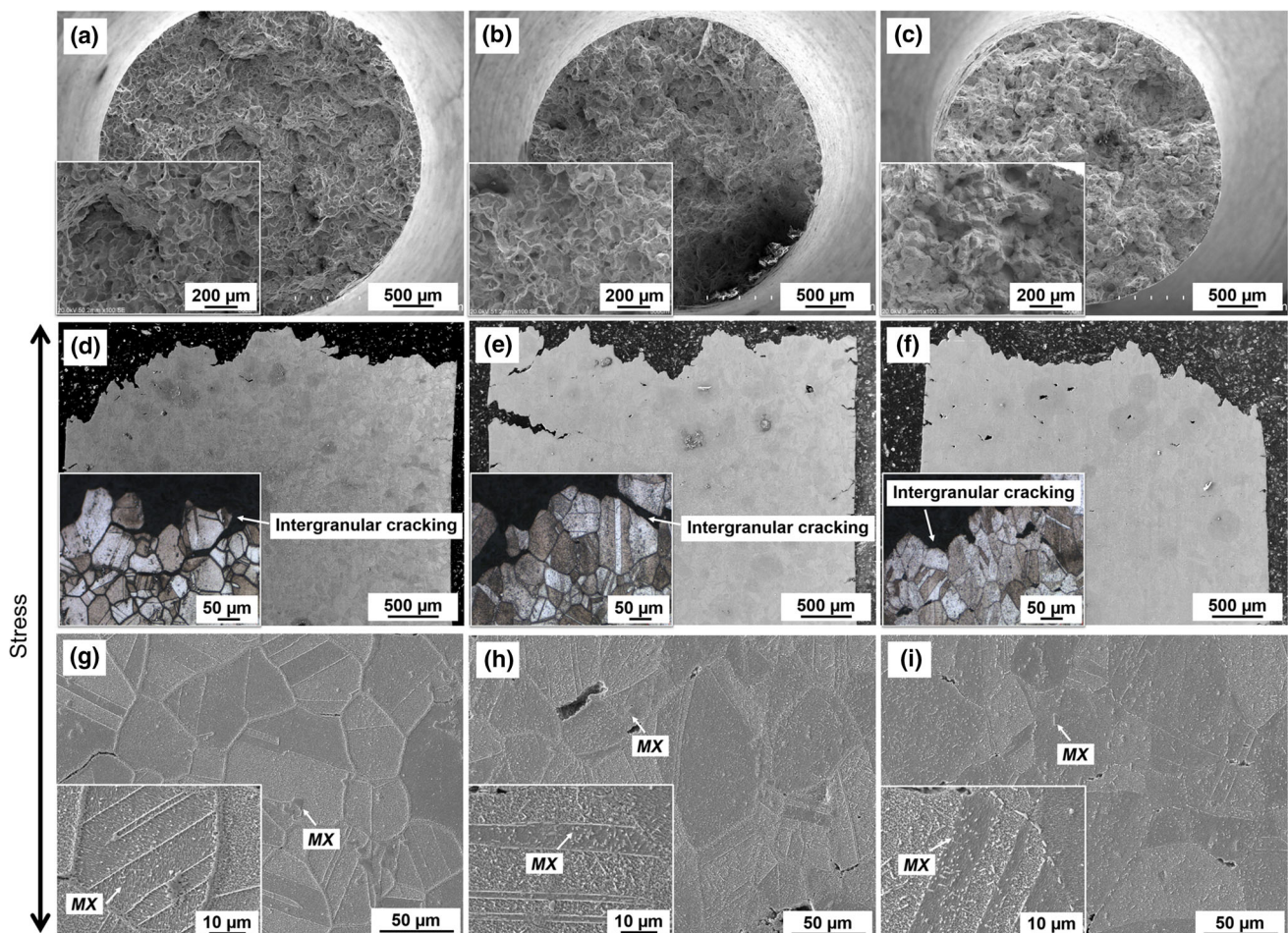


Fig. 10 Fracture surfaces **a–c** and longitudinal section of fracture surfaces at low **d–f**, high **g–i** magnification of T8 alloy crept at 650 °C/250 MPa **a, d, g**, 700 °C/180 MPa **b, e, h**, 750 °C/130 MPa **c, f, i**

continuous $M_{23}C_6$ carbides along grain boundaries) and the matrix can be the preferred sites for nucleation of the microcracks, and the precipitates along the interface are easily peeled off from the matrix [29]. As a result, the grain boundaries are widened and coarsened with increasing rupture life. The stress ruptured sample tested at 750 °C/130 MPa was exposed to high temperature for 567 h, resulting in a significant oxidation of the fracture surface (Fig. 10c). Oxides are inclined to distribute along grain boundaries and weaken the grain boundary strength and facilitate the occurrence of the intergranular fracture further during stress rupture test.

4 Conclusions

The effect of heat treatment on the microstructures and mechanical properties of a newly developed austenitic heat resistant steel (T8 alloy) have been studied in this work. From the current study, the main conclusions can be drawn as follows:

1. The microstructures of the alloy after solution treatment consist of austenite matrix phase of $Cr_{0.19}Fe_{0.7}Ni_{0.11}$ (atomic ratio) and primary bulk MX phases. MX phases (M is mostly substituted for Nb) distribute both inside the grains and at the grain boundaries.
2. After aging treatment, $M_{23}C_6$ carbides (M is mostly substituted for Fe, Cr) precipitate along the grain boundaries and nanoscale MX phases precipitate inside the grains and no any harmful phases appears in the alloy. With increasing the aging temperature and time, the morphology of $M_{23}C_6$ carbides changes from semi-continuous chain to continuous network.
3. Compared with a commercial HR3C alloy, T8 alloy has comparable yield strength and ultimate tensile strength. However, the elongation of T8 alloy is lower than that of HR3C alloy during high-temperature tensile test. The stress rupture resistance of T8 alloy is better than that of HR3C alloy.
4. Transgranular cracking is the dominant cracking mode of the alloy at room temperature. The increase in the test temperature leads to the decrease in both strength and ductility. The precipitation of $M_{23}C_6$ carbides along the austenite grain boundaries occurs during the tensile tests at 650 and 700 °C, which results in the dominating presence of typical intergranular cracking. Typical intergranular cracking is the dominant cracking mode of the alloy during all stress rupture tests.

Acknowledgements This work was supported financially by the National Natural Science Foundation of China (Nos. 11332010,

51671189 and 51701210) and the Project from China Huaneng Group Co. Ltd. (No. ZD-15-HJK02).

References

- [1] S. Guan, C.Y. Cui, Acta Metall. Sin. (Engl. Lett.) **28**, 1083 (2015)
- [2] G. Stein-Brzozowska, D.M. Flórez, J. Maier, G. Scheffknecht, Fuel **108**, 521 (2013)
- [3] R. Viswanathan, J.F. Henry, J. Tanzosh, G. Stanko, J. Shingledecker, B. Vitalis, R. Purgert, J. Mater. Eng. Perform. **14**, 281 (2005)
- [4] R. Viswanathan, K. Coleman, U. Rao, Int. J. Press. Vessels Pip. **83**, 778 (2006)
- [5] R. Viswanathan, W. Bakker, J. Mater. Eng. Perform. **10**, 81 (2001)
- [6] I.G. Wright, A.S. Sabau, R.B. Dooley, Mater. Sci. Forum **595–598**, 387 (2008)
- [7] T.B. Gibbons, Trans. Indian Inst. Met. **66**, 631 (2013)
- [8] Y.H. Zhou, Y.C. Liu, X.S. Zhou, C.X. Liu, J.X. Yu, Y. Huang, H.J. Li, W.Y. Li, J. Mater. Sci. Technol. (2017). <https://doi.org/10.1016/j.jmst.2017.01.025>
- [9] C. Fang, Y.S. He, K.B. Yoo, J.S. Jung, K.S. Shin, Key Eng. Mater. **727**, 22 (2017)
- [10] Y. Gao, C. Zhang, X. Xiong, Z. Zheng, M. Zhu, Eng. Fail. Anal. **24**, 26 (2012)
- [11] J.B. Yan, Y.F. Gu, F. Sun, Y.X. Xu, Y. Yuan, J.T. Lu, Z. Yang, Y.Y. Dang, Mater. Sci. Eng. A **675**, 289 (2016)
- [12] Y.Y. Fang, J. Zhao, X.N. Li, Acta Metall. Sin. (in Chinese) **46**, 844 (2010)
- [13] J.B. Yan, Y.F. Gu, J.T. Lu, Energy Mater. **31**, 389 (2015)
- [14] X. Bai, J. Pan, G. Chen, J. Liu, J. Wang, T. Zhang, W. Tang, Mater. Sci. Technol. **30**, 205 (2014)
- [15] L.Q. Cui, H.H. Su, J.J. Yu, J.L. Liu, T. Jin, X.F. Sun, Mater. Sci. Eng. A **696**, 323 (2017)
- [16] X.B. Zhao, Y.Y. Dang, H.F. Yin, J.T. Lu, Y. Yuan, Z. Yang, J.B. Yan, Y.F. Gu, Prog. Nat. Sci. **26**, 204 (2016)
- [17] H. Wang, C.Q. Cheng, J. Zhao, Z. Yang, Acta Metall. Sin. (in Chinese) **51**, 920 (2015)
- [18] Z.F. Peng, W. Ren, C. Yang, F.Y. Chen, H.G. Liu, F.F. Peng, M.Q. Song, Acta Metall. Sin. (in Chinese) **51**, 1325 (2015)
- [19] B. Wang, Z.D. Liu, S.C. Cheng, C.M. Liu, J.Z. Wang, Prog. Nat. Sci. **21**, 765 (2014)
- [20] J.M. Zhang, Y. Zhang, K.W. Xu, J. Cryst. Growth **285**, 427 (2005)
- [21] J.B. Yan, Y.F. Gu, F. Sun, Y. Michinari, Z.H. Zhong, Y. Yuan, J.T. Lu, Mater. Sci. Eng. A **639**, 15 (2015)
- [22] J. Genée, L. Signor, P. Villechaise, Mater. Sci. Eng. A **701**, 24 (2017)
- [23] Z.F. Zhang, Z.G. Wang, Acta Metall. **51**, 347 (2003)
- [24] T.S. Cao, X.D. Fang, C.Q. Cheng, J. Zhao, Acta Metall. Sin. (in Chinese) **50**, 1343 (2014)
- [25] H. Mats (ed.), translated by H.Y. Lai, G.X. Liu, Alloy Diffusion and Thermodynamic (Metallurgical Industry, Beijing, 1984) (**in Chinese**)
- [26] J. Xie, J.J. Yu, X.F. Sun, T. Jin, Y. Sun, Acta Metall. Sin. (in Chinese) **4**, 458 (2015)
- [27] Z. Zhang, Z. Hu, H. Tu, S. Schmauder, G. Wu, Mater. Sci. Eng. A **681**, 74 (2016)
- [28] C.Z. Zhu, Y. Yuan, P. Zhang, Z. Yang, Y.L. Zhou, J.Y. Huang, H.F. Yin, Y.Y. Dang, X.B. Zhao, J.T. Lu, J.B. Yan, C.Y. You, Metall. Mater. Trans. A **49**, 434 (2017)
- [29] P. Ou, L. Li, X.F. Xie, J. Sun, Acta Metall. Sin. (Engl. Lett.) **28**, 1336 (2015)